

RESEARCH LETTER

10.1002/2015GL065623

Key Points:

- The origin of water vapor rings in tropical cold pools is explained
- Surface latent heat fluxes explain water vapor rings
- Implications for parameterizations of cold pool effects in GCMs

Supporting Information:

- Texts S1 and S2 and Figures S1 – S4

Correspondence to:

W. Langhans,
wlanghans@lbl.gov

Citation:

Langhans, W., and D. M. Romps (2015), The origin of water vapor rings in tropical oceanic cold pools, *Geophys. Res. Lett.*, *42*, 7825–7834, doi:10.1002/2015GL065623.

Received 31 JUL 2015

Accepted 2 SEP 2015

Accepted article online 7 SEP 2015

Published online 25 SEP 2015

The origin of water vapor rings in tropical oceanic cold pools

Wolfgang Langhans¹ and David M. Romps^{1,2}

¹Earth Sciences Division, Lawrence Berkeley National Laboratory, Berkeley, California, USA, ²Department of Earth and Planetary Science, University of California, Berkeley, California, USA

Abstract Tropical deep convection over the ocean is found to grow preferentially from thermodynamically preconditioned regions of high specific humidity and, thus, high moist static energy. For this reason, rings of enhanced specific humidity at the leading edges of evaporatively driven cold pools have recently received considerable attention. The prevailing theory explains these rings by the water vapor source from the evaporation of rain drops below cloud base. Their origin is studied in this letter using large-eddy simulations of individual cumulus clouds that rise into a tropical atmosphere over ocean. It is demonstrated that—in contrast to this theory—water vapor rings are primarily explained by surface latent heat fluxes rather than by the evaporation of rain. This finding implies that conceptual models used in subgrid-scale parameterizations of deep convection should consider the formation of rings of increased specific humidity by the cold-pool-induced enhancement of surface fluxes.

1. Introduction

The presence of cold pools within the planetary boundary layer (PBL) over tropical oceans is crucial for the interaction between the PBL and the free troposphere through their impact on deep convection. The modulation of deep convection by cold pool dynamics has commonly been hypothesized to result from two processes: (a) the mechanical lifting of ambient air at the leading edge of cold pools as known from squall line dynamics [e.g., Moncrieff and Liu, 1999; Droegemeier and Wilhelmson, 1985; Rotunno et al., 1988] and (b) the preconditioning of the boundary layer for deep convection through cold pool induced enhancement of the moist static energy inside the PBL [Tompkins, 2001a, 2001b, the latter will be referred to as TO1].

The latter thermodynamic argument is based on the observation that cold pools exhibit rings of enhanced water vapor content and thus high moist static energy within their leading edges. These rings of enhanced water vapor content are visible from horizontal distributions of near-surface water vapor mixing ratios. They have been observed in gust fronts over tropical oceans [Addis et al., 1984] and have been described in various cloud-resolving and large-eddy simulations of deep tropical convection and precipitating trade wind cumuli [e.g., TO1; Xue et al., 2008; Khairoutdinov et al., 2009; Moeng et al., 2009; Moeng and Arakawa, 2012; Seifert and Heus, 2013; Torri et al., 2015].

Even if convective updrafts do not originate from preconditioned air inside an active cold pool (as argued by TO1), the positive moisture anomaly carried near the edges of recovering cold pools will later favor the triggering upon collision with a more active (i.e., younger) cold pool. This is described in TO1, who found that convection grows from PBLs with a preexisting vapor anomaly of about $+1 \text{ g kg}^{-1}$. The observed vapor rings are of relevance also as they may eventually cluster to larger moist patches [Schlemmer and Hohenegger, 2014] and trigger relatively wide—thus less entraining and deeper—clouds [Boing et al., 2012]. Several other studies demonstrated that deep convective updrafts over tropical oceans preferentially grow from anomalously moist parts of the boundary layer [Kingsmill and Houze, 1999; Seifert and Heus, 2013; Li et al., 2014; Torri et al., 2015]. Understanding the mechanisms behind the formation of these vapor rings is thus critical in understanding the influence of cold pools on deep convection. Although some convection parameterizations in global climate models (GCMs) account for the mechanical lifting by cold pools [Qian et al., 1998; Grandpeix and Lafore, 2010; Rio et al., 2013], air is generally modeled as being lifted from the unperturbed (i.e., environmental) part of the boundary layer without accounting for the effects of these vapor rings.

Moreover, despite the agreement on the relevance of these moist anomalies, different explanations were proposed for the origin of these rings. The prevailing hypothesis proposed by TO1 is that these rings form due to the evaporation of raindrops within the subcloud layer before the downdraft reaches the PBL. This theory

is supported by earlier observations of moistening of the subcloud layer by rain evaporation in a severe thunderstorm over the high plains [Betts, 1984]. In line with TO1, Seifert and Heus [2013] argue that evaporation of rain is key to the existence of these vapor rings. In contrast, Li *et al.* [2014] argue that evaporation of rain does not contribute to the anomalous moisture. To seed even more confusion, Li *et al.* [2014] and Schlemmer and Hohenegger [2014] conclude that in contrast to TO1, the enhanced vapor content is found *outside* of cold pools. This underlines the incongruity of previous explanations. On top of that, as pointed out by Schlemmer and Hohenegger [2015], a considerable fraction of such moisture anomalies could also originate from surface latent heat fluxes.

In this paper we seek a physical explanation of the origin of these vapor rings. More specifically, we seek to answer the following questions:

1. What is the origin of water vapor rings in tropical cold pools?
2. What are the individual contributions from evaporation of rain, surface latent heat fluxes, and the existing (i.e., prerin) PBL moisture anomaly?
3. Are the underlying physics in line with the conceptual ideas proposed by TO1?

To address these questions, we carry out large-eddy simulations and study the vapor sources using passive and active tracers of water vapor mass (see section 2). The simulations are motivated by atmospheric conditions commonly observed in radiative-convective equilibrium (RCE) over tropical oceans.

2. Numerical Setup

2.1. General Description

Numerical simulations are carried out using Das Atmosphärische Modell (DAM) [Romps, 2008]. DAM solves the compressible equations in flux form using a split-explicit [Klemp *et al.*, 2007] total-variation-diminishing (TVD) third-order Runge-Kutta (RK3) discretization in time [Shu and Osher, 1988]. Advection is discretized using a third-order upstream scheme and a positive-definite flux limiter [Thuburn, 1996] is applied to the moisture scalars. Following the concept of implicit LES [e.g., Margolin *et al.*, 2006], no subgrid-scale (SGS) turbulence closure is applied. The lateral boundary conditions are periodic.

A no-slip bottom boundary condition is applied and surface drag and sensible and latent heat fluxes are parameterized by bulk transfer laws using a drag coefficient of $C_d = 1.5 \times 10^{-3}$. If not mentioned otherwise, the surface moisture flux is parameterized as $\rho \overline{q'_v w'}|_s = -C_e |\mathbf{u}|_1 (q_v|_1 - q_v^*|_{\text{sst}})$ with $C_e = C_d$, with $q_v^*|_{\text{sst}}$ the saturation specific humidity for a sea surface temperature (SST) of 300 K and with index 1 denoting variables on the first model level.

The microphysical mass exchange rates among six water classes are parameterized using the Lin-Lord-Krueger one-moment bulk scheme [Lin *et al.*, 1983; Lord *et al.*, 1984; Krueger *et al.*, 1995] with minor adaptations as described by Langhans *et al.* [2015]. The bulk formulation distinguishes between six water classes: water vapor, cloud liquid water, cloud ice, rain, snow, and graupel.

2.2. Simulations

Single cumulus clouds are simulated in this study similar to the ones investigated by Langhans *et al.* [2015]. These clouds are forced from an initially axisymmetric “bubble” perturbation in the center of the numerical domain and rise into an atmosphere at rest. The advantage of this configuration is that the emerging cold pool remains quasi-axisymmetric without any collisions with other cold pools as it would be in simulations of RCE. Motivated by cold pools commonly observed in RCE, the initialized background temperature and specific humidity profiles $T_0(z)$ and $q_{v0}(z)$ are taken from previously conducted RCE runs over an SST of 300 K [see Romps and Kuang, 2011, section 3].

We focus on simulating the period of cold pool initiation and propagation. The domain and grid setup are thus tailored to achieve high resolution inside the boundary layer with a relatively coarse and inexpensive resolution above. The dimensions of the numerical domain are $(L_x, L_y, L_z) = (20, 20, 14.1)$ km. A five-layer structure is used to distribute levels in the vertical. Three sections with constant grid spacings δz of 10, 190, and 610 m, respectively, are separated by two sections that allow for smooth transitions based on tanh functions. The interfaces between the layers are located at 400, 3400, 5300, and 9300 m. The lowermost layer with $\delta z = 10$ m fully includes the emerging cold pools. The horizontal grid spacing is 50 m. The RK3 dynamics are solved using an adaptive time stepping to satisfy a maximum local Courant-number of 0.5.

A reference simulation, R1, and a sensitivity experiment R2 are presented in this letter, and additional sensitivity experiments are presented in the supporting information. Moist convection in R1 is initiated from an anomalously warm and moist boundary layer that exhibits a Gaussian-distributed perturbation of $q'_{v0} = 1 \text{ g kg}^{-1}$ with a half width of 3 km. This moisture anomaly is thought to represent the moisture excess caused by an older cold pool and the chosen scale, and magnitude is in line with findings in TO1 (his Figure 7) and others (see section 1). The sensitivity to this initialized moisture perturbation is tested in run R2 which starts without this moisture perturbation.

To kick off convection, a small-scale temperature perturbation of magnitude $\delta T = 1 \text{ K}$ is prescribed in both R1 and R2, as

$$T(r, z) = T_0(z) + (\delta T + \zeta) \exp \left[-(r/r_b)^2 - (z/z_b)^2 \right], \quad (1)$$

with $r = \sqrt{x^2 + y^2}$, height z , $r_b = 1000 \text{ m}$, $z_b = 500 \text{ m}$, and random perturbations $\zeta \in [-0.05, 0.05]$. In case of R1, the q_v perturbation is added as

$$q_v(r, z) = q_{v0}(z) + q'_{v0} \exp \left[-(r/R_b)^2 - (z/Z_b)^2 \right], \quad (2)$$

with $q'_{v0} = 10^{-3} \text{ g g}^{-1}$, $R_b = 3000 \text{ m}$, and $Z_b = 500 \text{ m}$. The cloud base is at around 500 m in these simulations, and the clouds reach maximum heights of about 11 km. Simulations are carried out for 2 h to capture the full life cycle of the cloud, including the dissipating stage and—most importantly—cold pool propagation.

Three further experiments were carried out to test the sensitivity to the surface transfer coefficient C_e . These are described in the supporting information (Text S1 and Figure S2 in the supporting information). One of them applies Monin-Obukhov similarity theory [Dyer and Hicks, 1970; Stull, 1988] to compute the surface latent heat flux. This experiment results in even larger surface latent heat fluxes than obtained by reference run R1.

The supporting information also contains a description of experiments aimed at testing the sensitivity to domain size and free-tropospheric relative humidity (see Text S2 and Figures S3 and S4). Increasing the latter yields stronger and longer-lived cold pools. Nevertheless, all these simulations yield the same conclusions as those drawn from R1 and R2.

2.3. Water Vapor Tracers

The individual contributions to the ring-shaped water vapor mass anomaly are identified here by advancing tracers of water vapor mass of different origin. To do so, tracer mass fractions are initialized at time $t_i = 1040 \text{ s}$, which is right before rain starts falling into the subcloud layer (i.e., pre-rain). A first (passive) tracer mass fraction q'_{pbl} represents the pre-rain PBL perturbation existing at time t_i . To define this perturbation, the water vapor field at time t_i is decomposed into a base state q_{base} and a perturbation q'_{pbl} . The former is horizontally uniform inside the subcloud layer and defined as

$$q_{\text{base}}(x, y, z, t_i) = \gamma(z)q_v(x, y, z, t_i) + [1 - \gamma(z)]q_v^\infty(z) \quad (3)$$

$$\gamma(z) = 0.5 + 0.5 \tanh [0.02(z - 500)], \quad (4)$$

with $q_v^\infty(z) = q_v(-L_x/2, -L_y/2, z, t_i)$ the specific humidity profile in a corner of the domain. The perturbation q'_{pbl} is defined as $q'_{\text{pbl}} = q_v - q_{\text{base}}$. Function $\gamma(z)$ goes from 0 to 1 across the cloud base at 500 m, such that q_{base} is horizontally uniform below cloud base and $q_{\text{base}} = q_v$ and $q'_{\text{pbl}} = 0$ above cloud base at time t_i . The base-state mass fraction q_{base} forms the second passive tracer to be advanced. Moreover, two active tracer mass fractions q'_{lh} and q'_{er} are advanced to study the water vapor mass due to surface latent heat fluxes and due to evaporation of rain, respectively. Both are initialized to zero at time t_i .

The mass M_χ of each tracer χ is advanced as

$$\frac{\partial(q_\chi \rho)}{\partial t} = -\frac{\partial(q_\chi \rho \mathbf{u})}{\partial \mathbf{x}} + S_\chi, \quad (5)$$

with tracer mass fraction $q_\chi = M_\chi / (M_a + M_v + M_l + M_s)$, density ρ , mass of dry air M_a , water vapor M_v , liquid water M_l , solid water M_s , and tracer mass source S_χ . The source term is zero for the two passive tracers

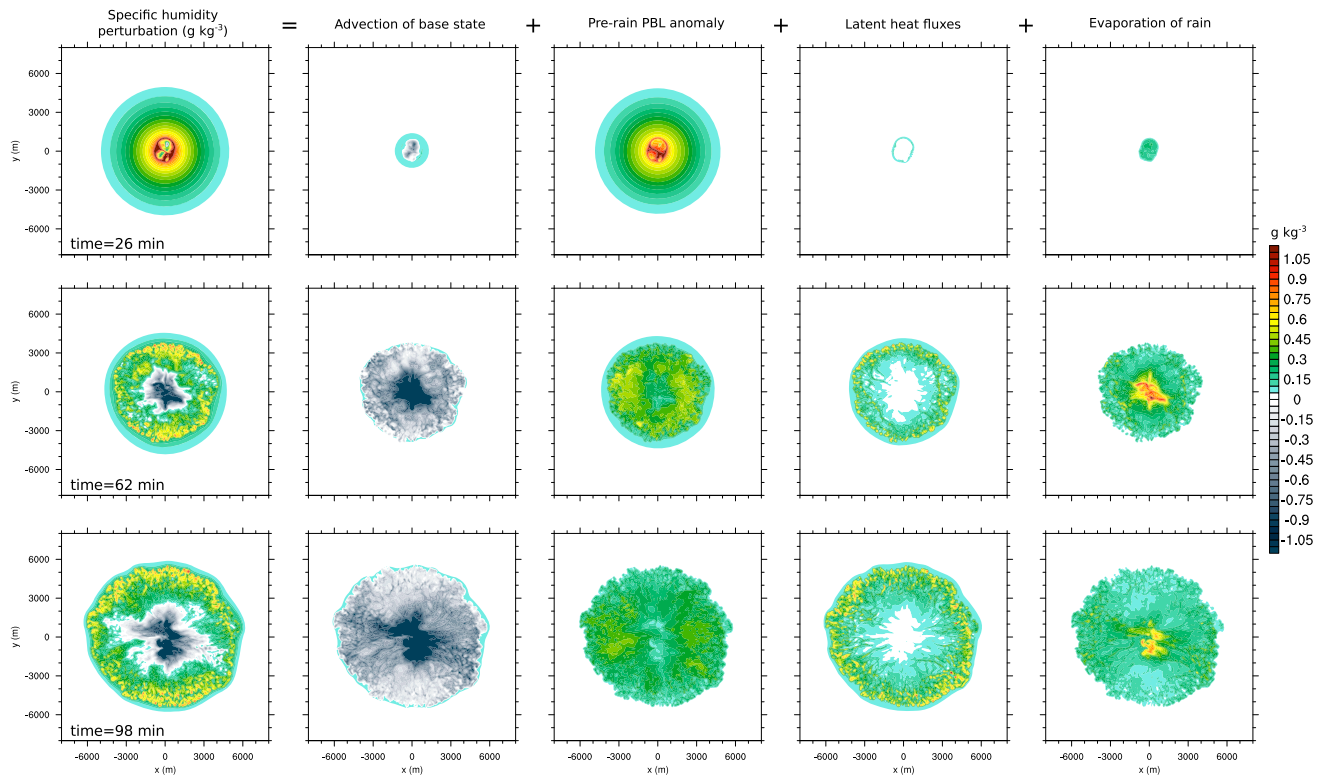


Figure 1. Decomposition of the (first column) perturbation water vapor mass fraction \overline{q}'_v into contributions from (second column) the base-state perturbation \overline{q}'_{base} , (third column) the prerain PBL anomaly \overline{q}'_{pbl} , (fourth column) latent heat fluxes \overline{q}'_{lh} , and (fifth column) evaporation of rain \overline{q}'_{er} . Distributions are from simulation R1 and shown after 26, 62, and 98 min. All quantities are computed as density-weighted vapor mass fractions for the lowest 100 m (see equation (6)). To obtain the perturbations in column 1 and 2, the far-field value of the base-state vapor mass fraction has been subtracted from the (first column) actual vapor mass fraction and from the (second column) base-state mass fraction. To a very good approximation, the sum of Figures 1 (second column) to 1 (fifth column) yields Figure 1 (first column).

q'_{base} and q'_{pbl} . The sources of the active tracers q'_{lh} and q'_{er} are the surface moisture flux convergence $S_{lh} = -\partial_z \rho q'_v w'|_s$ and the evaporation of rain $S_{er} = \rho E$, respectively.

We find that, at any time, the sum of q'_{base} , q'_{pbl} , q'_{lh} , and q'_{er} is almost identical to q'_v . The difference is significantly smaller than the water vapor perturbations we are interested in, confirming that surface latent heat fluxes and evaporation of rain are the only sources of relevance to the water vapor budget of cold pools in our simulations.

3. The Origin of Water Vapor Rings

3.1. Horizontal Distributions

Our simulations reveal considerable agreement with both previous observational and modeling studies of cold pools formed by tropical convection [e.g., *Young et al., 1995; TO1; Moeng et al., 2009; Zuidema et al., 2012; Torri et al., 2015; Feng et al., 2015*]. The cold pool simulated by R1 reaches a radius of about 7 km at the end of the simulation. In agreement with modeled cold pools in *Feng et al. [2015]* (see their Figure 6), average propagation speeds of the leading edge are about 1.5 m s^{-1} , the potential temperature depression in the center reaches from about -1.4 K initially to 0.0 K in the recovering stage, and the lifetime is about 1.5 h. The evolution of the radial velocity and the potential temperature are illustrated in Figure S1 of the supporting information. In particular agreement with previous modeling studies, distinct water vapor rings appear near the edge of radially spreading cold pools with specific humidities about 0.6 to 1.0 g kg^{-1} higher than in the unperturbed PBL away from the cold pool. To illustrate this and to identify the origin of these rings, we show density-weighted vapor mass fractions for the lowest 100 m, defined as

$$\overline{q}'_v = \frac{\int_0^{100\text{m}} dz' \rho(z') q'_v(z')}{\int_0^{100\text{m}} dz' \rho(z')}, \quad (6)$$

with $q'_v(x, y, z) = q_v(x, y, z) - q_v^\infty(z)$ a perturbation with respect to the far-field environment at time t_i . Analogously, average mass fractions are computed for the base-state perturbation $q'_{\text{base}} = q_{\text{base}} - q_v^\infty$, for the pre-rain PBL perturbation q'_{pbl} , for the latent heat flux perturbation q'_{lh} , and for the perturbation q'_{er} due to evaporation. The evolution of these average mass fractions is illustrated for R1 in Figure 1 by showing snapshots after 26, 62, and 98 min. To very good approximation, the actual perturbation of the vapor mass fraction shown in the first column results from the sum of the individual perturbations shown in the other columns.

During the early stage, at $t = 26$ min, the water vapor ring consists mostly of water vapor mass that existed already in the PBL before the onset of rainfall. The pre-rain PBL water vapor mass gets displaced laterally by the approaching dry air from aloft. At that time, the contributions from latent heat fluxes and from evaporation of rain are very small ($\leq 0.2 \text{ g kg}^{-1}$) inside regions with anomalously high vapor contents. The water vapor mass originating from rain peaks inside the cold pool and is collocated with the negative perturbation due to the downward advection of the base state.

The vapor perturbation from surface fluxes grows rapidly in time and, by $t = 62$ min, has reached peak magnitudes larger than those due to the pre-rain PBL anomaly. Then, only the water vapor mass from surface fluxes causes a distinct narrow ring-like anomaly. The largest mass fractions from evaporated rain are carried in the dry air mass that sunk down from aloft. The water vapor mass from evaporation thus peaks in the dry center of the cold pool with a relatively homogeneous mass distribution toward the outer edge. The pre-rain PBL perturbation gets dispersed radially outwards in time leading to an increasing areal coverage and to decreasing peak perturbations.

3.2. Vertical Distributions

To better understand the transport and origin of water vapor mass inside the cold pool, we analyze the average vertical distribution of water vapor density and its individual contributions in a next step. We first identify the radius at the leading edge of the cold pool $R(\varphi)$ for each azimuth angle φ . This gives a normalized radius $r^* = r/R$ for each grid column. Averaging is then applied over grid points that fall into the same r^* bins. This way, we avoid the blurring that would result from azimuthal averaging over r bins. At a given time, $R(\varphi)$ is here identified based on a filtered version of the kinetic energy field $E_w(\varphi, r) = 0.5w(\varphi, r)^2$ at $z = 15$ m. $R(\varphi)$ is taken as the maximum radius at which $E_w(\varphi, r)$ exceeds a threshold value. This method takes advantage of the lifting that occurs right in front of the cold pool, and $r^* = 1$ thus lies slightly ahead of the cold pool edge.

Figure 2 shows the obtained r^* - z distributions of water vapor density ($\rho_v = q_v \rho$; gray shading) for the same three time steps after 26, 62, and 98 min. Also shown are contours of the three tracer mass density distributions due to latent heat fluxes ($\rho'_{\text{lh}} = q'_{\text{lh}} \rho$; orange), evaporation of rain ($\rho'_{\text{er}} = q'_{\text{er}} \rho$; blue), and the pre-rain PBL water vapor perturbation ($\rho'_{\text{pbl}} = q'_{\text{pbl}} \rho$; red). These are contoured every 0.2 kg^{-1} (line labels are multiplied by 10). The average R is indicated on top of each panel.

During the early stage, at $t = 26$ min, the downdraft air undercuts the boundary layer air mass. The displaced air indeed carries the largest moisture content but not—as previously argued by TO1 and others—due to evaporative moistening but because the PBL was relatively moist in the first place. The water vapor mass from evaporation that is carried by air between the leading edge and the center ($\sim 0.2 \text{ g kg}^{-1}$) is considerably smaller than the pre-rain water vapor perturbation carried in the leading edge ($\sim 1.2 \text{ g kg}^{-1}$). The contribution from surface fluxes is also small at that time. It peaks near the surface close to the leading edge.

Later, after 62 and 98 min, the perturbation is mostly made up by water vapor mass that was supplied by surface latent heat fluxes. The latter cause a distinct perturbation near the leading edge with considerable vertical extent. In line with laboratory flows of density currents [e.g., Simpson and Britter, 1979], the near-surface flow inside the cold pool is considerably faster (about twice; see Figure S1) than the propagation speed of the leading edge. This leads to the enhancement of surface fluxes as seen previously from observations [Johnson and Nicholls, 1983; Addis et al., 1984; Young et al., 1995; Zuidema et al., 2012; Yokoi et al., 2014; Feng et al., 2015] and modeling studies [e.g., TO1; Redelsperger et al., 2000; Moeng et al., 2009; Feng et al., 2015] and to the transport toward and into the leading edge of the cold pool. At $t = 98$ min, the pre-rain PBL moisture has been lofted off the ground and significantly dispersed with minor contributions near the leading edge. The bulk of the evaporated rain mass trails behind the leading edge of the cold pool with small contributions to the low-level perturbation near $r^* = 1$. Note also that the vapor mass perturbation is clearly carried inside the cold pool and not outside or ahead of the leading edge as argued by Schlemmer and Hohenegger [2014] and Li et al. [2014].

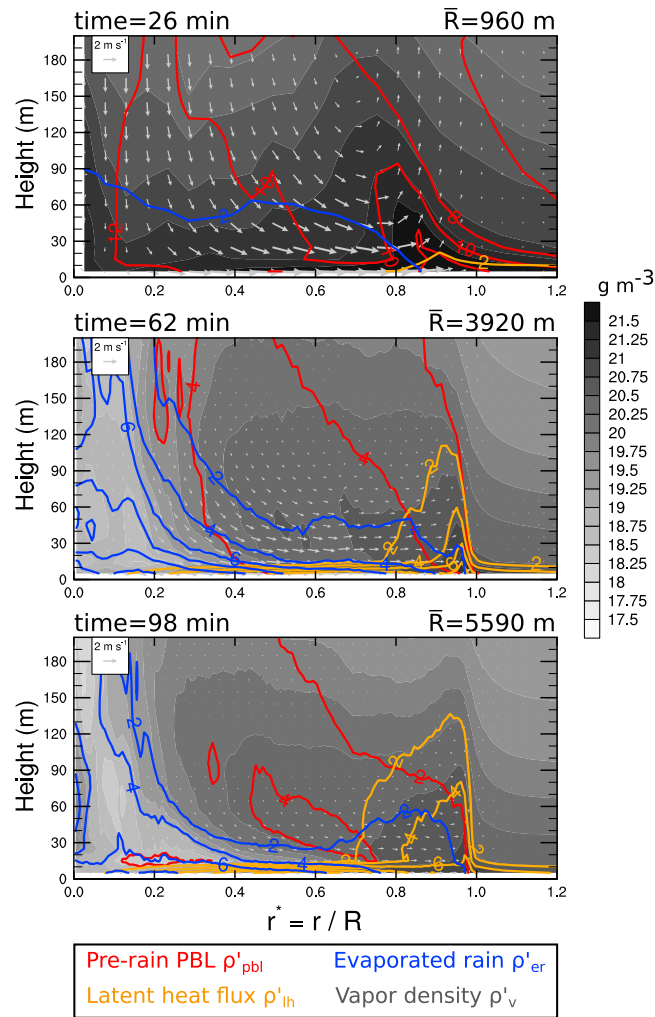


Figure 2. Azimuthally averaged r^* - z distributions of the water vapor density ρ_v (g m^{-3} ; gray shading) and of the individual perturbations due to latent heat fluxes ρ'_{lh} (orange contours), due to evaporation of rain ρ'_{er} (blue contours), and due to the prerain PBL anomaly ρ'_{pbl} (red contours) are shown for simulation R1 after 26, 62, and 98 min. The three perturbations are contoured every 0.2 g m^{-3} starting at 0.2 g m^{-3} (line labels are multiplied by 10). Vectors illustrate the average velocity field. A normalized radial distance $r^* = r/R$ has been computed first for each grid column with R the radius at the leading edge of the cold pool determined as described in the text. Averaging is then performed over r^* bins of width $dr^* = 50\text{m}/\bar{R}$ with \bar{R} the average R , which is indicated on top of each panel.

4. PBL Premoistening by Evaporating Rain?

Apparently, the evaporation of rain explains only a small fraction of the water vapor perturbation near the leading edge of cold pools. This is in sharp contrast to the prevailing theory developed by TO1 which relates the water vapor rings to the evaporation of rain drops in the subcloud layer during the time period before the dry downdraft air gets injected into this subcloud layer. A necessary condition for the validity of this theory is that there is sufficient evaporation of rain drops before the original subcloud layer air gets replaced by dry downdraft air from aloft. In other words, the time t_{req} required to moisten the subcloud layer by about $\delta r_v = 0.7 \text{ g kg}^{-1}$ (the maximum magnitude of anomalies reached inside the vapor ring; see Figure 1) has to be equal or smaller than the time t_{exp} during which the original subcloud layer air is exposed to rain drops. The subcloud layer will get squashed outside of the rain shaft by the approaching downdraft air. The latter thus sets t_{exp} .

It is demonstrated here that the ratio $t_{\text{req}}/t_{\text{exp}}$ is around three, even if an upper bound on t_{exp} is considered. An upper bound on t_{exp} is obtained as the time it takes an air parcel to sink from cloud base to the ground if it experiences only the minimal negative buoyancy due to the weight of condensate. Additional factors—which

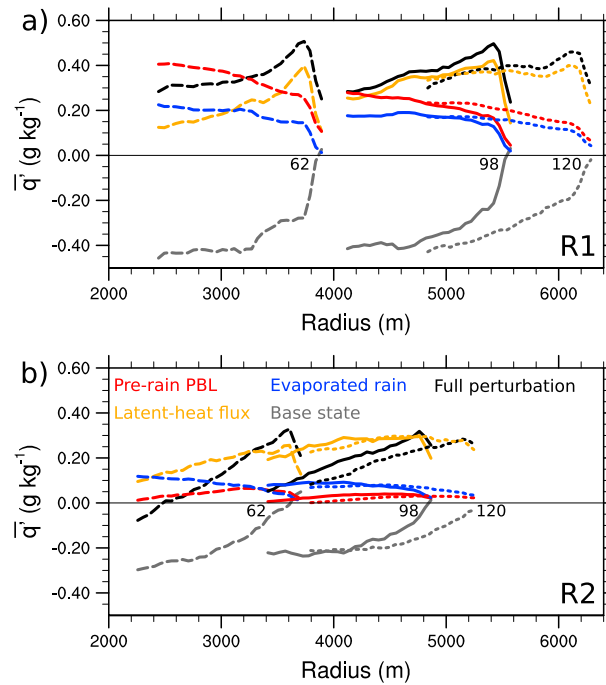


Figure 3. The \overline{q}'_v perturbations in the lowest 100 m (see also Figure 1) have been averaged in r^* space (see text for explanation) and are shown here for the outermost 1.5 km of the cold pool after (long dashed) 62, (solid) 98, and (short dashed) 120 min for (a) R1 and (b) R2. The perturbations were mapped back to radial distance using the average cold pool radius R at each time. At each time, the outermost data point corresponds to $r^* = 1$. The color code used for the perturbations is explained by the legend in Figure 3b.

decrease t_{exp} —such as the additional acceleration due to evaporation of liquid water or an existing downdraft at cloud base are neglected. Starting from a zero velocity at cloud base, the downdraft velocity (defined to be negative downward) is assumed to evolve according to the plume model of *Simpson and Wiggert* [1969], which has been applied previously to updrafts [*Jakob and Siebesma*, 2003; *Siebesma et al.*, 2003; *Gregory*, 2001] and downdrafts *Park* [2014], as

$$\frac{dw}{dt} = 0.5 \frac{dw^2}{dz} = aB + b\epsilon w^2. \quad (7)$$

In line with our desire to obtain an upper bound on t_{exp} , this model accounts for the adverse pressure gradient due to the arising inertial pressure and considers the drag due to lateral mixing. Following *Gregory* [2001] and *Jakob and Siebesma* [2003], we use $a = 1/3$ and $b = 2$. A constant negative buoyancy B is assumed that results only from condensate loading in the rain shaft below cloud base, such that $B = -gr_t/(1 + r_t)$ with g as the gravitational acceleration, r_l as the rain mixing ratio, and $r_t = r_v + r_l$ as the total water mixing ratio. The analytical solution for $w(z)$ is given in the appendix. Given $w(z)$, the time t_{exp} it takes to sink from $z = h$ to $z = 0$ is obtained by integrating $dt = w(z)^{-1} dz$, which gives

$$t_{\text{exp}} = \frac{1}{\sqrt{-B}\sqrt{ab\epsilon}} \tanh^{-1} \left(\sqrt{1 - e^{-2bh}} \right). \quad (8)$$

For a cloud base at $h = 500$ m and a typical value of the fractional entrainment rate $\epsilon = 0.5 \cdot 10^{-3} \text{ m}^{-1}$, one yields exposure times $t_{\text{exp}} = [350, 303, 271]$ s for the simulated range in rain mixing ratios of $r_l = [3, 4, 5]$ g kg⁻¹.

The required time t_{req} is given as $t_{\text{req}} = \delta r_v / \overline{E}$ with \overline{E} a vertically averaged evaporation rate inside a rain shaft in the subcloud layer. The latter is typically $0.8 \cdot 10^{-6} \text{ s}^{-1}$ in R1, yielding $t_{\text{req}} = 875$ s. Thus, $t_{\text{req}}/t_{\text{exp}}$ ranges between 2.5 and 3.2 for the specified range of rain mixing ratios. This simple estimate shows that—at best—only about one third of the anticipated δr_v can result from the evaporation of rain below cloud base. These numbers agree fairly well with our reference simulation which showed an evaporative water vapor source of about 0.2 g kg^{-1}

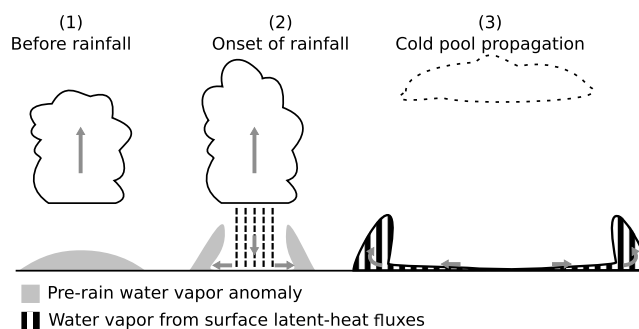


Figure 4. Schematic of the processes responsible for water vapor rings in tropical cold pools. (1) A water vapor perturbation exists below cloud base before rainfall sets in. Deep convective clouds rise from subcloud layers that are relatively moist due to, e.g., the vapor ring of an older cold pool. Even without a preexisting vapor ring, the prerin moisture excess below cloud base can result solely from enhanced surface fluxes during the early convergent period of cumulus growth. (2) The weight of rain drops is sufficient to maintain a downdraft that displaces the sub-cloud layer out of the rain shaft such that the exposure time of the subcloud layer to rain evaporation is short. The displaced and undercut air mass is relatively moist primarily due to the prerin water vapor anomaly; the source from rain evaporation remains secondary. (3) The cold pool spreads radially and surface latent heat fluxes continuously supply water vapor mass that gets fluxed toward and into the leading edge of the cold pool.

(see Figure 1) before air gets displaced laterally by the downdraft. Note also that a sensitivity experiment in which the evaporation of rain had been switched off resulted in the same dynamics in the subcloud layer during this initial stage of rainfall onset. Thus, the acceleration that squashes the subcloud air aside is indeed maintained by condensate loading rather than by the evaporation of rain drops.

5. Sensitivity to Initial PBL Moisture

The evaporation rate E of rain drops in the subcloud layer is largely controlled by relative humidity. Then, what if moist convection forms from a drier subcloud layer? Will the source from rain drop evaporation increase due to larger evaporation rates?

To test this, we analyze simulation R2 and again decompose the water vapor perturbation in the lowest 100 m into its different origins. The individual perturbations have been averaged in r^* space and are shown in Figure 3 for the outermost 1.5 km of the cold pool for both R1 and R2 after 62, 98, and 120 min. In R1 the averaged perturbation is 0.5 g kg^{-1} (Figure 3a) and evaporation of rain makes up less than a third of this perturbation. Again, the contribution from the surface latent heat fluxes is largest.

In line with *Droegemeier and Wilhelmson* [1985] (their section 5b), the drier initial boundary layer in R2 leads to weaker convective precipitation and thus to less evaporation and a weaker cold pool. Even though R2 is initialized without a PBL moisture anomaly, surface latent heat fluxes during the convergent period of convective growth form a weak prerin moisture anomaly below the cloud (see Figure 3b). This surface flux contribution to the prerin anomaly is even larger than in R1 (not shown), simply because R2 is drier than R1 and the surface latent heat fluxes scale with the moisture gradient at the surface (see section 2.1). For this reason, the prerin subcloud layer in R2 is not as dry as would be expected in the absence of this feedback. On top of that, rain mixing ratios r_l in the rain shaft are smaller than in R1 (not shown). Overall, the increase of E due to a smaller r_v is even overcompensated by the decrease due to smaller r_l . The ratio of $t_{\text{req}}/t_{\text{exp}}$ in R2 remains close to the one in R1 as both t_{req} and t_{exp} increase. As a result, the evaporative contribution to the water vapor perturbation is again insignificant in R2. As in R1, surface latent heat fluxes are the key player.

6. Conclusions

Rings of enhanced water vapor concentrations are associated with the leading edges of cold pools over tropical oceans. The idealized simulations of single cold pools carried out in this letter replicate this observation for an atmosphere initialized with thermodynamic profiles from radiative-convective equilibrium. In contrast to the prevailing theory, the findings presented herein show that surface latent heat fluxes are the primary cause for such ring-shaped water vapor anomalies inside the leading edge of a cold pool. The evaporation of rain drops below cloud base is found to be secondary since the subcloud layer is not exposed long enough

to the rain shaft before it gets displaced by the approaching dry downdraft air. The subcloud air which gets displaced by the downdraft is indeed relatively moist but not—as previously believed—due to rain drop evaporation but simply because deep convection grows from a relatively moist sub-cloud layer in the first place. Figure 4 summarizes the processes relevant during different stages of the cold pool's life cycle.

To advance the parameterization of cold pool effects on deep convection in GCMs, it thus appears key to represent the effects of surface latent heat fluxes within conceptual models for subgrid-scale convection. Based on our results, a parameterization should account for the enhanced latent heat fluxes into the cold pool and the subsequent mass transport into the cold pool edges. Future research needs to establish a conceptual model for the evolution of the magnitude of these water vapor rings. On top of that, the effects of enhanced water vapor content on, e.g., convective inhibition, need to be considered to account for the modified lifting trajectories of such thermodynamically conditioned air parcels.

Appendix A: Analytical Solution for $w(z)$

For constant b , ϵ , a , and B the analytical solution to (7) is

$$w(z) = -\sqrt{w(h)^2 e^{-2b\epsilon(h-z)} - \frac{aB}{b\epsilon} [1 - e^{-2b\epsilon(h-z)}]}, \quad (\text{A1})$$

with $0 \leq z \leq h$, h the height at cloud base, and $B \leq 0$.

Acknowledgments

This work was supported by the U.S. Department of Energy's Atmospheric System Research, an Office of Science, Office of Biological and Environmental Research program, and by the Scientific Discovery through Advanced Computing (SciDAC) program funded by U.S. Department of Energy Office of Advanced Scientific Computing Research and Office of Biological and Environmental Research, under contract DE-AC02-05CH11231. This research used computing resources of the National Energy Research Scientific Computing Center (NERSC), which is supported by the Office of Science of the U.S. Department of Energy under contract DE-AC02-05CH11231, and computing resources of the Extreme Science and Engineering Discovery Environment (XSEDE), which is supported by National Science Foundation grant OCI-1053575. W.L. likes to thank N. Jeevanjee for helpful discussions. Profiles used to initialize DAM are available from the corresponding author.

The Editor thanks three anonymous reviewers for their assistance in evaluating this paper.

References

- Addis, R. P., M. Garstang, and G. D. Emmitt (1984), Downdrafts from tropical oceanic cumuli, *Boundary Layer Meteorol.*, **28**, 23–49.
- Betts, A. K. (1984), Boundary layer thermodynamics of a high plains severe storm, *Mon. Weather Rev.*, **112**, 2199–2211.
- Boing, S. J., H. J. J. Jonker, A. P. Siebesma, and W. W. Grabowski (2012), Influence of the subcloud layer on the development of a deep convective ensemble, *J. Atmos. Sci.*, **69**, 2682–2698.
- Droegemeier, K. K., and R. B. Wilhelmson (1985), Three-dimensional numerical modeling of convection produced by interacting thunderstorm outflows. Part I: Control simulation and low-level moisture variations, *J. Atmos. Sci.*, **42**, 2381–2403.
- Dyer, A. J., and B. B. Hicks (1970), Flux-gradient relationships in the constant flux layer, *Q. J. R. Meteorol. Soc.*, **96**, 715–721.
- Feng, Z., S. Hagos, A. K. Rowe, C. D. Burleyson, M. N. Martini, and S. P. de Szoeke (2015), Mechanisms of convective cloud organization by cold pools over tropical warm ocean during the AMIE/DYNAMO field campaign, *J. Adv. Model. Earth Syst.*, **7**, 1–25.
- Grandpeix, J.-Y., and J.-P. Lafore (2010), A density current parameterization coupled with Emanuel's convection scheme. Part I: The models, *J. Atmos. Sci.*, **67**, 881–897.
- Gregory, D. (2001), Estimation of entrainment rate in simple models of convective clouds, *Q. J. R. Meteorol. Soc.*, **127**, 53–72.
- Jakob, C., and A. P. Siebesma (2003), A new subcloud model for mass-flux convection schemes: Influence on triggering, updraft properties, and model climate, *Mon. Weather Rev.*, **131**, 2765–2778.
- Johnson, R. H., and M. E. Nicholls (1983), A composite analysis of the boundary-layer accompanying a tropical squall line, *Mon. Weather Rev.*, **111**, 308–319.
- Khairoutdinov, M. F., S. K. Krueger, C.-H. Moeng, P. A. Bogenschutz, and D. A. Randall (2009), Large-eddy simulation of maritime deep tropical convection, *J. Adv. Model. Earth Syst.*, **1**, 15, doi:10.3894/JAMES.2009.1.15.
- Kingsmill, D. E., and R. A. Houze (1999), Thermodynamic characteristics of air flowing into and out of precipitating convection over the west Pacific warm pool, *Q. J. R. Meteorol. Soc.*, **125**, 1209–1229.
- Klemp, J. B., W. C. Skamarock, and J. Dudhia (2007), Conservative split-explicit time integration methods for the compressible nonhydrostatic equations, *Mon. Weather Rev.*, **135**, 2897–2913.
- Krueger, S. K., Q. A. Fu, K. N. Liou, and H. N. S. Chin (1995), Improvements of an ice-phase microphysics parameterization for use in numerical simulations of tropical convection, *J. Appl. Meteorol.*, **34**, 281–287.
- Langhans, W., K. Ye, and D. M. Romps (2015), Lagrangian investigation of the precipitation efficiency of convective clouds, *J. Atmos. Sci.*, **72**, 1045–1062.
- Li, Z., P. Zuidema, and P. Zhu (2014), Simulated convective invigoration processes at trade wind cumulus cold pool boundaries, *J. Atmos. Sci.*, **71**, Corrigendum, 71, 4710.
- Lin, Y.-L., D. F. Richard, and H. D. Orville (1983), Bulk parametrization of the snow field in a cloud model, *J. Appl. Meteorol.*, **22**, 1065–1092.
- Lord, S. J., H. E. Willoughby, and J. M. Piotrowicz (1984), Role of a parameterized ice-phase microphysics in an axisymmetric, nonhydrostatic tropical cyclone model, *J. Atmos. Sci.*, **41**, 2836–2848.
- Margolin, L. G., W. J. Rider, and F. F. Grinstein (2006), Modeling turbulent flow with implicit LES, *J. Turbulence*, **7**, 1–27.
- Moeng, C.-H., and A. Arakawa (2012), Representation of boundary layer moisture transport in cloud-resolving models, *Mon. Weather Rev.*, **140**, 3682–3698.
- Moeng, C.-H., M. A. LeMone, M. F. Khairoutdinov, S. K. Krueger, P. A. Bogenschutz, and D. A. Randall (2009), The tropical marine boundary layer under a deep convection system: A large-eddy simulation study, *J. Adv. Model. Earth Syst.*, **1**, 16, doi:10.3894/JAMES.2009.1.16.
- Moncrieff, M. W., and C. Liu (1999), Convection initiation by density currents: Role of convergence, shear, and dynamical organization, *Mon. Weather Rev.*, **127**, 2455–2464.
- Park, S. (2014), A Unified Convection Scheme (UNICON). Part I: Formulation, *J. Atmos. Sci.*, **71**, 3902–3930.
- Qian, L., G. S. Young, and W. M. Frank (1998), A convective wake parameterization scheme for use in general circulation models, *Mon. Weatehr Rev.*, **126**, 456–469.
- Redelsperger, J., F. Guichard, and S. Mondon (2000), A parameterization of mesoscale enhancement of surface fluxes for large-scale models, *J. Atmos. Sci.*, **57**, 402–421.
- Rio, C., et al. (2013), Control of deep convection by sub-cloud lifting processes: The ALP closure in the LMDZ5B general circulation model, *Clim. Dyn.*, **40**, 2271–2292.

- Romps, D. M. (2008), The dry-entropy budget of a moist atmosphere, *J. Atmos. Sci.*, *65*, 3779–3799.
- Romps, D. M., and Z. Kuang (2011), A transilient matrix for moist convection, *J. Atmos. Sci.*, *68*, 2009–2025.
- Rotunno, R., J. B. Klemp, and M. L. Weisman (1988), A theory for strong, long-lived squall lines, *J. Atmos. Sci.*, *45*, 463–485.
- Schlemmer, L., and C. Hohenegger (2014), The formation of wider and deeper clouds as a result of cold-pool dynamics, *J. Atmos. Sci.*, *71*, 2842–2858.
- Schlemmer, L., and C. Hohenegger (2015), Modifications of the atmospheric moisture field as a result of cold-pool dynamics, *Q. J. R. Meteorol. Soc.*, doi:10.1002/qj.2625.
- Seifert, A., and T. Heus (2013), Large-eddy simulation of organized precipitating trade wind cumulus clouds, *Atmos. Chem. Phys.*, *13*, 5631–5645.
- Shu, C. W., and S. Osher (1988), Efficient implementation of essentially non-oscillatory shock-capturing schemes, *J. Comput. Phys.*, *77*, 439–471.
- Siebesma, A. P., et al. (2003), A large eddy simulation intercomparison study of shallow cumulus convection, *J. Atmos. Sci.*, *60*, 1201–1219.
- Simpson, J., and V. Wiggert (1969), Models of precipitating cumulus towers, *Mon. Weather Rev.*, *97*, 471–489.
- Simpson, J. E., and R. E. Britter (1979), The dynamics of the head of a gravity current advancing over a horizontal surface, *J. Fluid Mech.*, *94*, 477–495.
- Stull, R. B. (1988), *An Introduction to Boundary Layer Meteorology*, 666 pp., Kluwer Acad., Boston, Mass.
- Thuburn, J. (1996), Multidimensional flux-limited advection schemes, *J. Comput. Phys.*, *123*, 74–83.
- Tompkins, A. M. (2001a), Organization of tropical convection in low vertical wind shears: The role of water vapor, *J. Atmos. Sci.*, *58*, 529–545.
- Tompkins, A. M. (2001b), Organization of tropical convection in low vertical wind shears: The role of cold pools, *J. Atmos. Sci.*, *58*, 1650–1672.
- Torri, J., Z. Kuang, and Y. Tian (2015), Mechanisms for convection triggering by cold pools, *Geophys. Res. Lett.*, *42*, 1943–1950, doi:10.1002/2015GL063227.
- Xue, H., G. Feingold, and B. Stevens (2008), Aerosol effects on clouds, precipitation, and the organization of shallow cumulus convection, *J. Atmos. Sci.*, *65*, 392–406.
- Yokoi, S., M. Katsumata, and K. Yoneyama (2014), Variability in surface meteorology and air-sea fluxes due to cumulus convective systems observed during CINDY/DYNAMO, *J. Geophys. Res. Atmos.*, *119*, 2064–2078, doi:10.1002/2013JD020621.
- Young, G. S., S. M. Perugini, and C. W. Fairall (1995), Convective wakes in the equatorial western Pacific during TOGA, *Mon. Weather Rev.*, *123*, 110–123.
- Zuidema, P., Z. Li, R. J. Hill, L. Bariteau, B. Rilling, C. Fairall, W. A. Brewer, B. Albrecht, and J. Hare (2012), On trade wind cumulus cold pools, *J. Atmos. Sci.*, *69*, 258–280.